PEMFC Transient Response Characteristics Analysis in Case of Temperature Sensor Failure

Authors:

Jaeyoung Han, Sangseok Yu, Jinwon Yun

Abstract:

In this study, transient responses of a polymer electrolyte fuel cell system were performed to understand the effect of sensor fault signal on the temperature sensor of the stack and the coolant inlet. We designed a system-level fuel cell model including a thermal management system, and a controller to analyze the dynamic behavior of fuel cell system applied with variable sensor fault scenarios such as stuck, offset, and scaling. Under drastic load variations, transient behavior is affected by fault signals of the sensor. Especially, the net power of the faulty system is 45.9 kW. On the other hand, the net power of the fault free system is 46.1 kW. Therefore, the net power of a faulty system is about 0.2 kW lower than that of a fault-free system. This analysis can help in understanding the transient behavior of fuel cell systems at the system level under fault situations and provide a proper failure avoidance control strategy for the fuel cell system.

PEMFC Transient Response Characteristics Analysis in Case of Temperature Sensor Failure

Jaeyoung Han [1], Sangseok Yu [2],* and Jinwon Yun [1],*

[1]   School of Mechanical & Automotive Engineering, Youngsan University, 288 Junam-ro,
     Yangsan-si 50510, Korea; hjyt11@ysu.ac.kr
[2]   Department of Mechanical Engineering, Chungnam National University, 99 Daehak-ro, Yuseong-gu,
     Daejeon 34134, Korea
*   Correspondence: sangseok@cnu.ac.kr (S.Y.); jwyun@ysu.ac.kr (J.Y.); Tel.: +82-42-821-5646 (S.Y.);
     +82-55-380-9541 (J.Y.); Fax: +82-42-822-5642 (S.Y.); +82-55-380-9249 (J.Y.)

Abstract: In this study, transient responses of a polymer electrolyte fuel cell system were performed to understand the effect of sensor fault signal on the temperature sensor of the stack and the coolant inlet. We designed a system-level fuel cell model including a thermal management system, and a controller to analyze the dynamic behavior of fuel cell system applied with variable sensor fault scenarios such as stuck, offset, and scaling. Under drastic load variations, transient behavior is affected by fault signals of the sensor. Especially, the net power of the faulty system is 45.9 kW. On the other hand, the net power of the fault free system is 46.1 kW. Therefore, the net power of a faulty system is about 0.2 kW lower than that of a fault-free system. This analysis can help in understanding the transient behavior of fuel cell systems at the system level under fault situations and provide a proper failure avoidance control strategy for the fuel cell system.

Keywords: fuel cell vehicle; dynamic system model; controller; fault scenario; fault tolerance control; thermal management system

---

1. Introduction

Proton exchange membrane fuel cells (PEMFC) have been considered the most promising type of fuel cells, which can be used as automotive power sources to replace conventional engines using gasoline and diesel [1–3]. Nowadays, most large automakers such as Hyundai, General Motors, Toyota, Ford, and other companies are developing fuel cell vehicles.

However, there are still many technical issues that have to be overcome before commercialization, including high cost and inadequate durability [4–7]. The transient responses of fuel cell systems are major problems that need to be solved before further commercialization of fuel cell technology [8–11]. Especially, in automotive fuel cells, the stack durability decreases due to frequent start-stop cycles and load variation [12,13]. In addition, a dynamic system model can help in the investigation of transient responses in the overall system or in individual subsystems. When there is an abrupt sensor failure in the system or balance of the plant (BOP), the actuator and the stack can indicate severe damage due to unbalanced temperature distribution or overheating in the stack. Moreover, in the event of fuel cell system failure, a deep understanding of fuel cell dynamic response will make it possible to improve fault tolerance controller design to rapidly avoid system damage. Consequently, successful investigation of transient response during sensor failure is critical to determine which parts of the subsystem are mainly affected by failure.

Various models have been designed as methods to investigate the transient response at the PEMFC system level. Tian et al. proposed a multi-physics transient model of PEM fuel cells using equivalent circuits. Authors developed three equivalent circuit models including electric, pneumatic, and thermal transient models. The transient model designed in this study was validated for steady-state and transient behaviors [14]. He et al. established a three-dimensional multiphase non-isothermal fuel cell model in which the effects of the geometric structure parameters of the cathode catalyst layer are investigated; however, only simplified three-dimensional transient representation was used [15]. Liu et al. investigated dynamic load characteristics for fuel cell durability; Liu et al. also looked at optimal control design and demonstrated the response characteristics of the balance of the plant, as well as the system dynamics performance. Liu et al. analyzed the distribution variation of the internal physical quantities at the system level. As a result, authors provided a theoretical basis for dynamic capacity optimization [16]. Using empirical fuel cell performance data, Messing et al. discussed the cathode electrode durability of PEMFCs and it was shown that the effect of the lower potential limit applied under load cycle changes. Finally, data from the cathode electrode durability model were compared with fuel cell stack durability data under different load cycle conditions [17]. Pan et al. investigated the PEMFC performance based on different flow fields to optimize the system efficiency; a novel design and modeling method are proposed in the Pan et al. study. Authors used a regression analysis to investigate the transient behavior [18]. Gwak et al. proposed a current-raising strategy to achieve rapid cell temperature rise for a stack; a three-dimensional, transient cold-start model was designed. However, the stack model is limited to the lumped channel model [19]. Murugesan et al. designed a semi-empirical dynamic fuel cell model to present dynamic phenomena related to water management. In general, water management such as membrane flooding and hydration has a great influence on stack dynamics. Murugesan et al. also investigated system performance according to water management at the stack level [20]. Lee et al. modelled a Ballard-Mark-V stack for underwater vehicles. A power converter device such as a DC-DC converter was employed to regulate the voltage at the desired value. In this paper, only oxygen was supplied to the air supply system, because underwater vehicles generally use oxygen [21]. Kim et al. developed a dynamic interactions model including heat and mass transfer models. Kim et al. also analyzed the dynamic behavior of a fuel cell vehicle with control of the blower and back pressure control valve and conducted a parametric study on the dynamic response of the fuel cell vehicle [22].

Moreover, there are studies on the transient behavior, a new approach for fuel cell systems to further improve system performance. Kim et al. proposed a start-up strategy to optimize fuel cell system performance. Kim et al. also conducted a parametric study on a self-humidified fuel cell system and investigated the dry start-up process under various ambient conditions [23]. Pan et al. developed a PEMFC model including water transfer model to analyze the variations of the voltage and the anode pressure by considering membrane water transfer. Authors also investigated the dynamics of the anode pressure under different opening areas of the purge valve [24]. Chen et al. suggested a gas purging method to remove excess water and avoid flooding and performance degradation of the stack; it was shown that the performance may eventually stabilize before the next purging begins [25].

Few studies have analyzed the transient responses of fuel cell vehicles under temperature sensor failure [26–28]. Especially, most previous studies investigated transient responses under fault-free conditions, and so they are still unsatisfactory for understanding the transient behavior in the interaction system. Therefore, for conditions of failure in the temperature sensors of the stack and coolant inlet, an understanding of the transient behavior in fuel cell systems, with respect to subsystems, remains needed.

The aim of this study is to understand the transient response phenomena in fuel cell systems, which are the results of interactions among system components, when a failure occurs in the temperature sensors of the stack and coolant inlet. First, we developed a dynamic fuel cell model at the system-level, including an air propulsion system (APS), fuel propulsion system (FPS), thermal management system (TMS), and controller. Our study used the lump stack model. Since our study focuses on the temperature of the stack and coolant inlet, the lump model was adapted to assume that the temperature of the stack is constant regardless of location. In addition, the lump model can reduce unnecessary computation time. TMS comprises a detailed radiator model, reservoir model, 3-way valve model, water pump model, radiator fan model, and controller. Notably, the temperatures for the reservoir and the fuel cell body are separated in our model. Sensor fault signals such as stuck, scaling, and offset were applied to the sensors of the stack and reservoir to analyze the transient behavior. Lastly, the effect of the fuel cell system was analyzed by examining the influence of the temperature sensor on failure of the stack and the reservoir. Moreover, better understanding of the transient behavior will help in the development of an optimal fault avoidance strategy for efficient fuel cell system operation.

This paper is organized as follows: Section 2 describes the development of the dynamic fuel cell system model including APS, FPS, and TMS. The fault scenarios are introduced in Section 3. Section 4 provides analysis of the simulation results and discusses the optimal strategy. Finally, the conclusions are summarized in Section 5.

2. Dynamic Model for the PEMFC

The following modeling assumptions were employed in the design of the fuel cell system:

(1)   The lumped model approach was used in this study for reducing computation load.
(2)   All gases were assumed to be ideal.
(3)   Operating stack temperature and coolant inlet is controlled at 70 °C.
(4)   The heat generated in the gas on the anode and the cathode sides was much smaller than the stack heat.
(5)   The water injected by the humidifier was in the form of vapor of latent heat.
(6)   Flow in the gas channel was fully developed laminar flow.
(7)   Liquid water transport along the stack channel is neglected.

2.1. Lumped Stack Model

As mentioned in the above introduction section, the lumped stack model was used. The lumped stack model consists of channels of anode and cathode, bipolar plate, end plate, gas diffusion layer (GDL), catalyst layer (CL), and membrane.

2.1.1. Anode Channel System

The hydrogen tank supplies hydrogen to the anode channel of the fuel cell. The inlet flow rate of the cathode can be instantaneously adjusted by a valve to keep the minimum pressure difference between the anode and cathode. Hydrogen is usually supplied from the injection pump to the cathode. However, if the pressure on the anode is larger than the pressure on the cathode, recirculation occurs. The cathode flow model consists of the mass flows of two elements. Two elements of the anode volume model are the vapor mass, $m_{v,an}$, and the hydrogen mass, $m_{H_2,an}$.

Their state equations are:

$$\dot{m}_{H_2,an} = \dot{m}_{H_2,an,in} - \dot{m}_{H_2,an,out} - \dot{m}_{H_2,an,react} \tag{1}$$

$$\dot{m}_{v,an} = \dot{m}_{v,an,in} - \dot{m}_{v,an,out} - \dot{m}_{v,mem} \tag{2}$$

where $m_{H_2,an,react}$ is the mass flow rate of reactive hydrogen in the anode, and $m_{v,membrane}$ is the mass flow rate of water through the membrane of the fuel cell.

2.1.2. Cathode Channel System

The cathode mass flow model describes the air flow behavior of the cathode in the fuel cell stack. The model is developed using thermodynamic and mass conservation principles. The cathode flow model consists of the mass flow of three elements. Similar to the anode flow model, levels of oxygen, nitrogen, and steam are determined by balancing the mass flow.

$$\dot{m}_{O_2,ca,st,ch} = \dot{m}_{O_2,ca,in,ch} - \dot{m}_{O_2,ca,out,ch} - \dot{m}_{O_2,ca,react,ch} \tag{3}$$

$$\dot{m}_{v,ca,st,ch} = \dot{m}_{v,ca,in,ch} - \dot{m}_{v,ca,out,ch} + \dot{m}_{v,mem,ch} + \dot{m}_{v,ca,gen,ch} - \dot{m}_{l,ca,out,ch} \tag{4}$$

$$\dot{m}_{N_2,ca,st,ch} = \dot{m}_{N_2,ca,in,ch} - \dot{m}_{N_2,ca,out,ch} \tag{5}$$

where $\dot{m}_{O_2,ca,react}$ is the mass flow rate of oxygen that reacted in the cathode, $\dot{m}_{v,ca,gen}$ is the mass flow rate of water generated by the reaction in the fuel cell, and $\dot{m}_{v,mem}$ is the mass flow rate of water through the fuel cell membrane.

2.1.3. Hydrogen & Oxygen Utilization Factor

In a proton exchange membrane fuel cell, current produced by the fuel cell depends on the mole numbers of reacted oxygen and hydrogen in the chemical reaction. In fact, the actual mass flow rate of the channel inlet is higher than the theoretical mass flow rate because oxygen and hydrogen are not 100% utilized. The mass flow rate of oxygen and hydrogen supplied to the channel is given by

$$\dot{m}_{air,ca,in} = \frac{I}{4F \times 0.21} \times n_{cell} \times M_{air} \times s_{sto,air} \tag{6}$$

$$\dot{m}_{air,ca,con} = \frac{I}{4F \times 0.21} \times n_{cell} \times M_{air} (consumed \ O_2 flow \ rate) \tag{7}$$

$$\dot{m}_{H_2,an,in} = \frac{I}{2F} \times n_{cell} \times M_{H_2} \times s_{sto,H_2} \tag{8}$$

$$\dot{m}_{H_2,an,con} = \frac{I}{2F} \times n_{cell} \times M_{H_2} (consumed \ H_2 flow \ rate) \tag{9}$$

2.1.4. Cell Voltage Model

The actual cell voltage is combined with irreversible losses, consisting of activation loss, concentration loss, and Ohmic loss. Hence, the actual cell operating voltage is lower than the theoretical cell operating voltage. The open circuit voltage is the maximum operating voltage (when no current is flowing) of a fuel cell and is determined by the chemical thermodynamics of the overall cell reaction. Thus, combing the open circuit voltage with the associated losses, the actual fuel cell operating voltage can be obtained as

$$E_{cell} = E_{Nern} - E_{act} - E_{ohm} - E_{con} \tag{10}$$

where E_{cell} is the cell voltage, E_{Nern} is the Nernst voltage, E_{act} is the activation overvoltage, E_{ohm} is ohmic overvoltage, and E_{con} is concentration overvoltage.

Open Circuit Voltage (OCV)

The Nernst's voltage can be expressed as [29]

$$E_{Nern} = \begin{aligned} &1.229 - (8.5 \times 10^{-3})(T_{cell} - 298.15) + 4.3085 \times 10^{-5} \\ &\times T_{cell} \times \ln(p_{H_2} \times 0.5 p_{O_2}) \end{aligned} \tag{11}$$

where T_{cell} is the cell temperature, p_{H_2} is the hydrogen partial pressure, and p_{O_2} is the oxygen partial pressure.

Activation Overvoltage

The activation losses are associated with reaction kinetics on the surface of the electrode. In order to activate the reaction, it is necessary to exceed the limits of the activation energy. The activation losses indicate the difference from the equilibrium needed for the reaction to start; this difference is caused by sluggish electrode kinetics. The activation loss can be obtained from [29].

$$E_{act} = \varphi_1 + \varphi_2 T_{cell} + \varphi_3 T_{cell}\left[\ln\left(C_{O_2}\right)\right] + \varphi_4 T_{cell}[\ln(j/n_{cell})] \tag{12}$$

where the φ values are turning factors, which are determined by experimental data; j is current density and n_{cell} is the number of cells in the stack.

Ohmic Overvoltage

Ohmic losses are caused by the electrons that flow through electrically conductive fuel cell components, such as gas diffusion layers and bipolar plates, and the resistance in the electrolyte. The ohmic overvoltage of the cell system can be obtained by [29].

$$E_{ohm} = j \times R_{mem} \tag{13}$$

where R_{mem} is the electric resistance in the membrane, determined by the following equation:

$$R_{mem} \int_{z=0}^{z=t_{mem}} \frac{1}{\sigma_{mem}} dz_{mem} \tag{14}$$

where σ_{mem} is the electric membrane conductivity, determined by the cell temperature and water activity.

$$\sigma_{mem}(T_{cell}, \lambda) = \exp\left[1268\left(\frac{1}{303} - \frac{1}{T_{cell}}\right)\right](0.005139\lambda - 0.00326) \tag{15}$$

Concentration Overvoltage

Concentration loss, also called mass transport loss, is the result of changes in the reactant concentration gradients on the electrode surface when the reactant is rapidly consumed by the electro chemical reaction in the electrode.

The concentration loss can be obtained by [29].

$$E_{con} = c \ln \frac{j_L}{j_L - j} \tag{16}$$

where j_L is the limiting current density.

2.1.5. Water Transport Model in the Membrane

The water concentration in the anode channel decreases due to the electro-osmotic drag that is the result of net water flux and drag coefficient, while the water concentration in the channel of the cathode is increased by the electro-osmotic drag. For this reason, there is a concentration difference between the anode and cathode. That is the reason for the back diffusion from the cathode to the anode. As a result, the water transport model must be designed to evaluate the water balance between the cathode and the anode. The water transport model in our study can be obtained by [30]. Table 1 shows the specifications of the fuel cell stack.

Table 1. Specifications of fuel cell stack.

Specification	Value	Unit
Fuel cell length	0.196	m
Fuel cell width	0.196	m
Membrane thickness	0.000108	m
Fuel cell temperature	70	°C
Coolant inlet temperature	60	°C
Number of cells in stack	381	NA

2.1.6. Heat Transfer and Energy Balance

Heat transfer and energy conservation are major factors used to evaluate the transient response characteristics when sensor failure occurs in the stack and cooling water. Hence, energy conservation values of a lumped transient stack model and a transient reservoir model were established as [30]

$$\rho_{grp}c_{p,grp}V_{cell}\frac{dT_{cell}}{dt} = \Delta H - W_{ele} - Q_{cool} - Q_{gas} - Q_{sur} \tag{17}$$

where $\Delta H = \sum_{in} \dot{m}h - \sum_{out} \dot{m}h$ is the enthalpy difference between the inlet flow rate and the outlet flow rate, W_{ele} is the electric work of a PEMFC stack produced by chemical reaction, Q_{cool} is the heat rejected to coolant, Q_{gas} is the heat rejected to bulk gases of the anode and cathode, Q_{sur} is the heat rejected to the surrounding, ρ_{grp} is the density of the graphite, $c_{p,grp}$ is the specific heat of the graphite, and V_{cell} is the unit cell volume.

The heat transfer to the bulk gas can be expressed as

$$Q_{gas} = \dot{m}_{gas}c_{p,gas}\left(T_{gas,in} - T_{gas,out}\right) \tag{18}$$

where

$$T_{gas,out} = T_{cell} + \left(T_{gas,in} - T_{cell}\right)\exp\left(-\frac{h_{gas}A_{gas}}{\sum \dot{m}_{gas,in}c_{p,gas}}\right) \tag{19}$$

A transient reservoir model is also designed to model the sensor failure. The coolant water in the channel of the stack and cooling compartment of the cooling circuit is considered a lumped mass. The lumped coolant temperature in the reservoir is given by

$$m_{cool}c_{p,rev}\frac{dT_{cool,in}(= dT_{rev})}{dt} = c_{p,cool}\dot{m}_{cool}(T_{mix} - T_{rev}) \tag{20}$$

where m_{cool} and $c_{p,rev}$ are the mass of the reservoir and specific heat of the reservoir, and $T_{cool,in}$ is the coolant inlet temperature entering the coolant channel in the stack. The coolant inlet temperature is the same as the reservoir temperature (T_{rev}). T_{mix} is the sum of the coolant outlet temperature through the channel of the stack and core of the radiator.

2.1.7. Cooling Compartments

To accurately investigate the transient response characteristics during sensor failure, it is very important to design the cooling compartments such as the coolant passages in the stack, radiator with an electric fan, and water pump with an electric motor. If a detailed cooling compartments model is not developed, it may be analyzed differently from the actual failure phenomenon. To reflect the actual failure phenomenon as much as possible, it is necessary to design an accurate and detailed cooling compartment model.

The outlet temperature at the cooling channel inside the cell is used to determine the coolant inlet temperature, cell temperature, and heat transfer coefficient through the channel. The coolant outlet temperature at the cooling channel can be calculated as [30]

$$T_{cool,out} = T_{cell} + \left(T_{cool,in} - T_{cell}\right)\exp\left(-\frac{h_{cool}A_{cool}}{\sum \dot{m}_{cool}c_{p,cool}}\right) \tag{21}$$

The heat transfer by convection to the coolant is given by

$$Q_{cool} = \dot{m}_{cool}c_{p,cool}\left(T_{cool,in} - T_{cool,out}\right) \tag{22}$$

where h_{cool} is the convective heat transfer coefficient of the coolant.

The heat transfer coefficient of the coolant can be determined by the Nusselt correlation under laminar flow condition. However, it is necessary to consider a turbulent regime to design the heat transfer coefficient, because this value depends on the amount of rejected heat. Therefore, heat transfer coefficient can be obtained as

$$h_{cool} = \frac{Nu \times k}{D} \tag{23}$$

$$Nu = \frac{(f/8)(\text{Re} - 1000)Pr}{1 + 12.7 \times (f/8)^{0.5}\left(Pr^{0.67} - 1\right)} \quad : 3000 \leq \text{Re} < 5 \times 10^6 \tag{24}$$

where k is the thermal conductivity, and D is the hydraulic diameter of the cooling channel.

The water pump and fan reject heat generated by the electrochemical reaction by regulating the coolant or air flow rate. In our study, the empirical model was used to determine the specifications of the fan and the water pump. The flow rate of the fan and the water pump is determined by a performance curve, determined by the motor speed and flow rate; there is also a module to determine pressure drops inside the cooling compartments. Therefore, the performance curve of the water pump and the radiator fan can be determined by

$$\Delta p_{fan} = A_1\left(\frac{\dot{m}_{air} \times 3600}{\rho_{air}}\right) + A_2\left(\frac{\dot{m}_{air} \times 3600}{\rho_{air}}\right)^2 + A_3\,(pa) : radiator \quad fan \tag{25}$$

$$\Delta p_{pump} = B_1\left(\frac{N}{3500}\right)^2 - B_2 \cdot \left(\frac{\dot{m}_{cool} \times 60000}{\rho_{cool}}\right)^2 (kPa) : water \quad pump \tag{26}$$

where Q is the flow rates of the air and the coolant, which are determined in terms of the pressure drop and the fan speed; N is the motor speed; and A_1, A_2, A_3, B_1, and B_2 are fitting factors.

In general, radiator models with fins have been widely used in vehicles to reject heat generated by heat sources. To accurately simulate the heat removal phenomenon generated from the stack, a louver fin radiator was developed in our study. In fact, to evaluate the performance of the cooling module with ram air resulting from vehicle speed, a detailed radiator model was designed in our previous study. The louver fin radiator model in our study can be obtained from [29].

3. Controller Design

The PI controller regulates the speed of the motor that drives the water pump, radiator fan, and opening angle of the three-way valve. A controller was installed in the nonlinear fuel cell to directly control the actuators. The two nonlinear thermal response models are models of fuel cell stack and water reservoir, and the actuators to control these are a three-way valve, water pump, and radiator fan. In addition, the temperature increase according to the power change from the outside was set as the disturbance. The controller detects the temperature of the water reservoir and the stack; it also detects the outlet temperature of the cooling water. Then, the required values for the actuators are sent to the system by the controller. In general, when designing a controller in the case of thermal systems, only proportional control and integral control are considered. The controller including proportional control and integral control can be expressed as

$$u(t) = \int \left(k_p + k_I\right)dt \tag{27}$$

Also, the schematic of the PI control response for the cooling system can be seen in Figure 1.
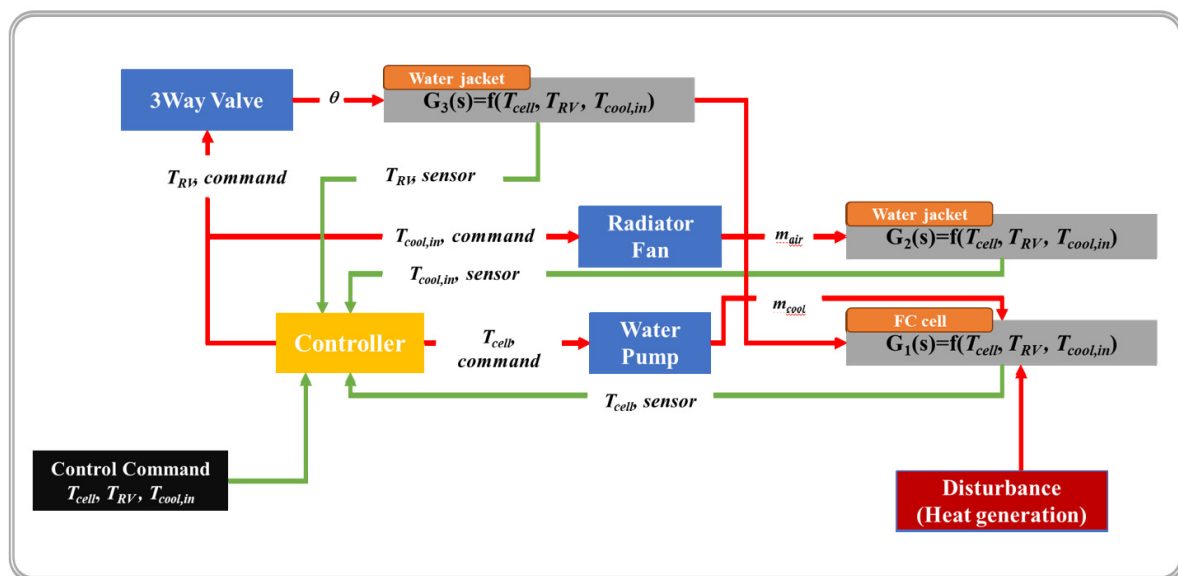
Figure 1. Schematic of PI control response for cooling system.

4. Results and Discussion

4.1. Fault Scenarios

In this section, we describe the dynamic response of the fuel cell system under load changes when a fault signal such as stuck, offset, or scaling is implemented by the sensor. The simulation was tested under step load changes. Before adding the step load, the operating conditions such as the temperature of the stack, coolant inlet, and ambient, as well as the humidity were set at 70 °C, 60 °C, 25 °C, and 100%, respectively. The step load profile of the current density is plotted in Figure 2, in which it can be seen that the load changed from 0.6 A/cm^2 to 0.74 A/cm^2 and 0.66 A/cm^2. Table 2 shows a summary of the fault scenarios implemented in this study.
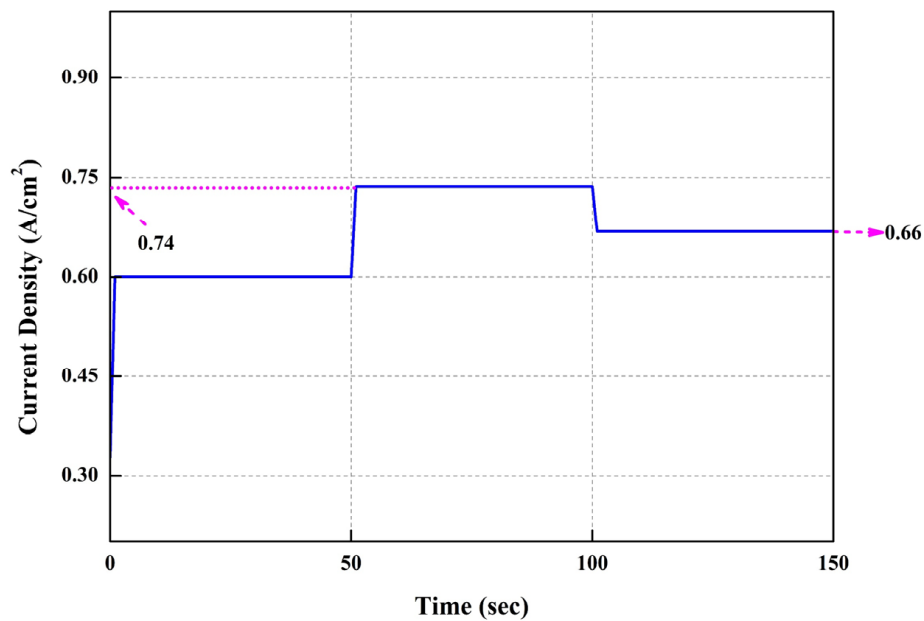
Figure 2. Scenarios of load profile (current density) in 150 s.

Table 2. Implemented fault scenario.

Fault Description	Fault Type	Magnitude
Stack sensor	Stuck	−45 °C
	Offset	−25 °C
	Scaling	50%
Coolant inlet sensor	Stuck	−10 °C
	Offset	−25 °C
	Scaling	50%

4.2. Fault Free PEMFC Dynamic Simulation

To investigate the transient responses in fault-free condition, a fuel cell system was simulated while subjected to a scenario of load profiles. A positive and a negative step were sequentially excited at intervals of 50 s, as shown in Figure 2.

As shown in Figure 3, the coolant flow rate through the water jacket, the air flow rate through the radiator grill, and the opening size of the three-way valve were intentionally changed to set values, along with the load, which was changed to satisfy the heat rejection capacity. The water flow rate, air flow rate, and opening area of the three-way valve were maintained at 0.24 kg/s, 0.8 kg/s, and 88% between t = 0 s and t = 50 s. Then, at t = 50 s, the water flow rate and air flow rate increased to 0.48 kg/s and 0.86 kg/s due to high heat generation. On the other hand, when the heat generation increases, the valve closes and coolant flows toward the radiator for rejection of the heat. Also, the water flow rate, air flow rate, and opening area of the three-way valve were changed to 0.36 kg/s, 0.87 kg/s, and 80%. To meet these conditions, the water pump, radiator fan, and three-way valve need to have fast transient responses. Also, heat transfer and cell voltage responses under fault free mode are displayed in Figure 3c,d.
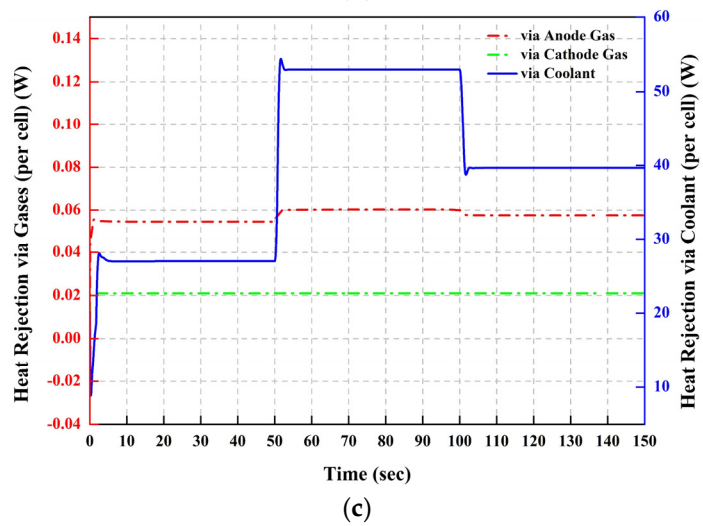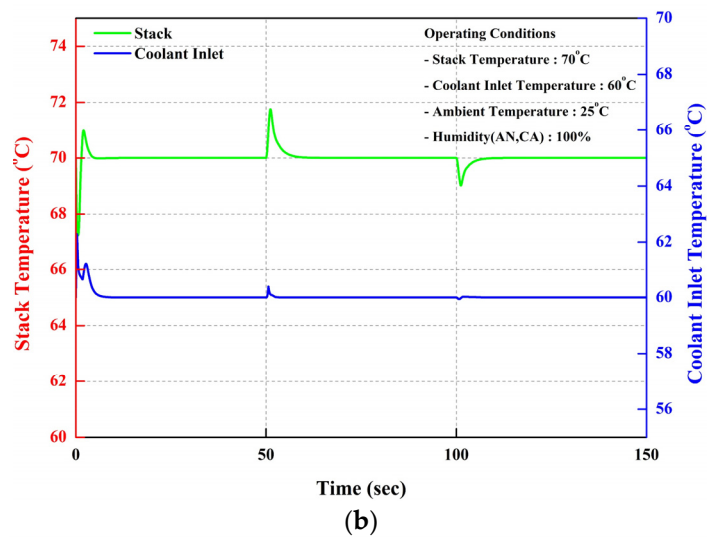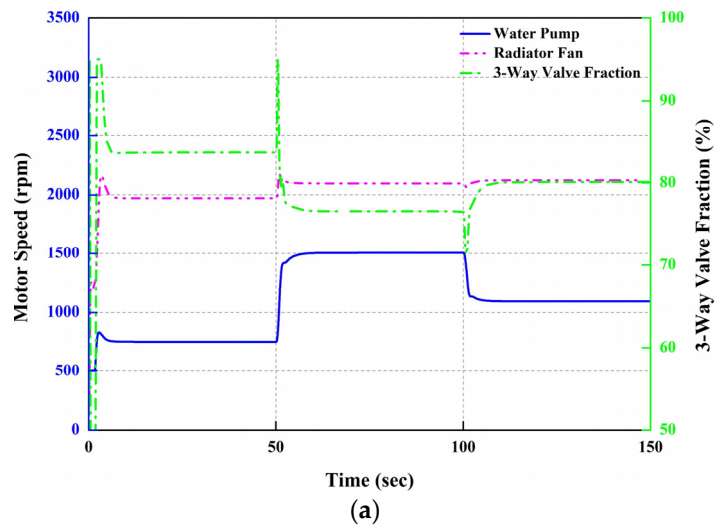
(**a**)

(**b**)

(**c**)

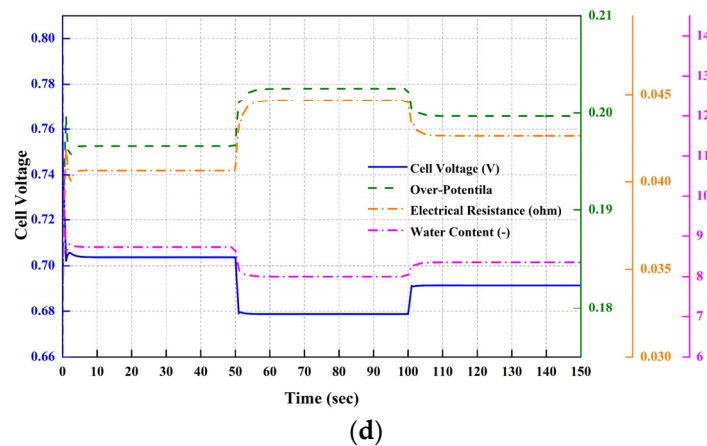**Figure 3.** *Cont.*

(**d**)

Figure 3. Dynamic responses of fuel cell system ((**a**) Thermal management system, (**b**) temperature of stack and coolant, (**c**) heat rejection in stack, (**d**) voltage responses).
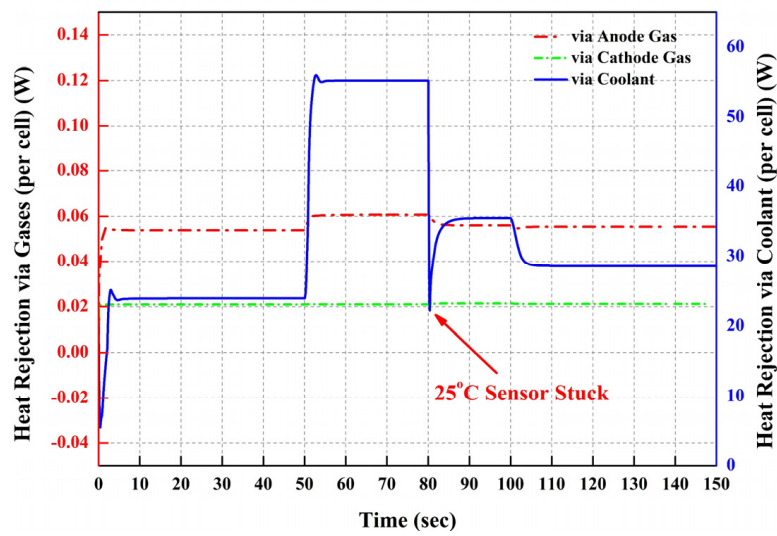
4.3. Stack Sensor Stuck

The dynamic effect of the fuel cell system under stuck fault in the temperature sensor was examined, as shown in Figure 4; the actual stack and coolant inlet temperature outputs and the sensor outputs of the stack and the coolant inlet temperature were recorded. The stack temperature sensor stuck fault (25 °C) was implemented at the time of 80 s. First, the actual stack temperature and actual coolant inlet temperature were screened; it can be observed from Figure 4a that the actual stack temperature value increased to 81.2 °C, while the actual coolant inlet temperature value was maintained at 60 °C, despite the sensor failure at the stack sensor, because of the continuous fan operation, as shown in Figure 4b. When the stuck fault occurs in the stack sensor, the water pump does not operate anymore because the sensor output of the stack is lower than the desired control temperature (70 °C), as shown in Figure 4b. Since the coolant inlet temperature sensor is normal, the coolant inlet temperature was maintained at the desired control target value (60 °C) by the radiator fan controller, even during stuck fault in the stack sensor. That is why the value of the actual stack temperature and the value of the stack temperature sensor are the same despite the occurrence of downshoot or overshoot at 80s, as shown in Figure 4a,c, which shows the dynamic responses of the heat rejection via gases and water coolant. It can be seen in Figure 4c that, at 80 s, the heat rejection via gases drops from 0.06 W to 0.058 W. This is because the stack temperature is higher than the temperature of both gases due to the stack sensor fault. Also, the heat rejection via coolant was decreased by the low coolant flow rate. When the stuck fault occurs in the stack sensor, the water pump does not operate anymore. For this reason, a small amount of coolant flows in the channel, because it is no longer working. This is because the sensor value is lower than the desired value in the controller. Figure 4d shows the dynamic responses of the cell voltage, over-potential, electric resistance, and water content corresponding to the stuck fault in stack sensor. It is clear that the output voltage changes after each load change. Then, when the stuck fault occurs in the stack sensor, the cell voltage increases slightly, which could result from the dependent effects of the stack temperature, water content, partial pressures of the reactant gases, and electrical capacitance. This is because the cell voltage is affected by the stack temperature, which can have a high value at high stack temperature. However, if the stack temperature increases above a critical value, the cell voltage decreases because of electrical resistance and over-potential. When the stack temperature increases, electrical resistance decreases. On the other hand, when the stack temperature decreases, electrical resistance increases. For this reason, if the stack temperature exceeds the critical temperature value, cell voltage decreases due to high electrical resistance.

(**a**)

(**b**)
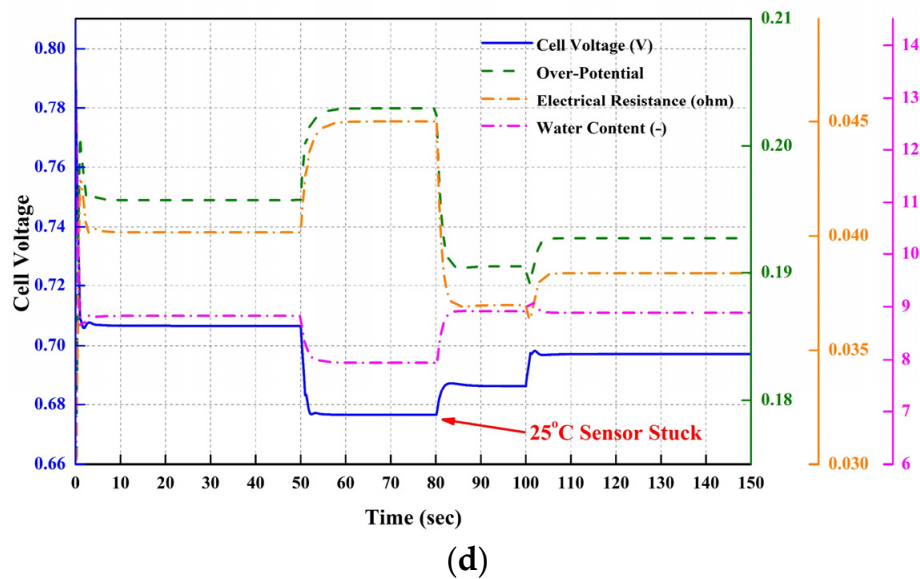

(**c**)

Figure 4. *Cont.*

(d)
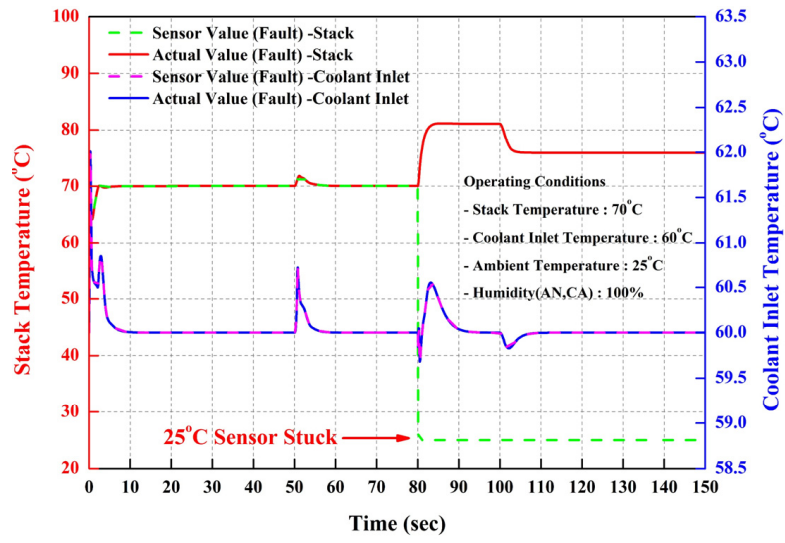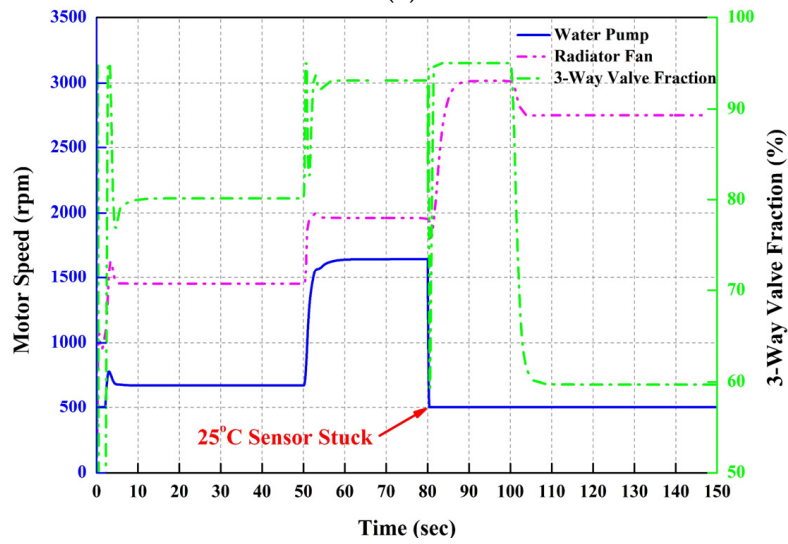
Figure 4. Transient sensor fault behavior in PEM fuel cell under sudden stack sensor stuck ((**a**) Temperature of stack and coolant inlet, (**b**) cooling components, (**c**) heat rejection in stack, (**d**) voltage responses).

4.4. Stack Sensor Scaling

The dynamic results of the fuel cell system with scaling fault on the stack temperature sensor were studied, with results shown in Figure 5. The actual output values of the stack temperature and coolant inlet temperature, the inlet temperature value of coolant sensor, and the sensor output of the stack coolant were obtained. The 50% scaling fault of the stack temperature sensor was applied at the time of 80 s. The actual stack temperature increased until 81.2 °C, while the actual inlet temperature of the coolant was kept as 60 °C, as can be seen in Figure 5a, because the radiator fan operated continuously, as shown in Figure 5b. When the 50% scaling fault of the stack sensor occurs, the value from the stack temperature sensor is still below 70 °C, which is the desired operation temperature of the stack. As a result, there is a trend similar to that of the stack stuck fault case, and the water pump for coolant flow is not running, as shown in Figure 5b. Nevertheless, the coolant inlet temperature was kept at the desired value of 60 °C by the radiator fan, according to the control logic that operates the radiator fan with the normal inlet temperature sensor of the coolant. This is how the actual stack temperature was maintained even though 50% stack sensor scaling occurred at 80 s, as shown in Figure 5b. Figure 5c shows the heat rejection from the stack by anode and cathode gases and coolant. The heat rejection by anode gas decreased because the stack temperature sensor was at 50% scaling fault. Because the water pump does not operate properly due to the stack temperature sensor 50% scaling fault, under lower flow rate of the coolant the heat rejection by coolant also decreased compared with that of the normal operation. Figure 5d shows the responses of the cell voltage, over-potential, electric resistance, and water content corresponding to the 50% scaling fault of the stack temperature sensor. The cell voltage change can be clearly seen and is affected by the stack operation temperature, as shown in Figure 5d. The 50% scaling fault of the stack temperature sensor caused cell voltage rise under higher operation temperature of the stack, which influenced the water content, partial pressure of reactant gases, and electrical capacitance. As a result, the stack operation temperature should be properly maintained.
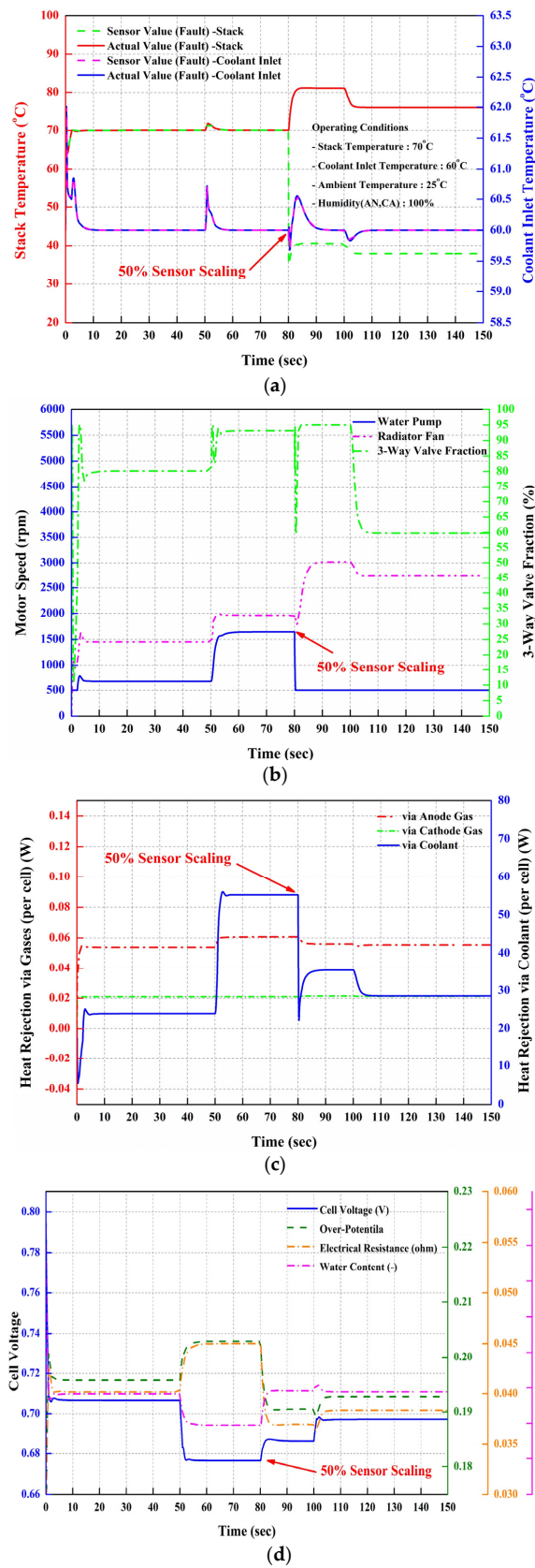
Figure 5. Transient sensor fault behavior in PEM fuel cell under sudden stack sensor scaling ((**a**) Temperature of stack and coolant inlet, (**b**) cooling components, (**c**) heat rejection in stack, (**d**) voltage responses).

4.5. Stack Sensor Offset

Figure 6 shows various values affected by the offset fault of the stack temperature sensor due to a problem in which the value of the sensor is 25 °C lower than the actual stack temperature. Comparisons between the actual results of the stack and coolant temperatures and the sensor results of the stack and coolant temperatures are shown in Figure 6a. The 25 °C offset fault of the stack temperature sensor starts at 80 s. Since the sensor has an error, the actual operation temperature of the stack increased to more than 80 °C, while the coolant inlet temperature was held at 60 °C. This is why the radiator fan started to run faster than in normal operation, as shown in Figure 6b. When a 25 °C offset fault of the stack temperature sensor occurs, the stack temperature sensor produces values that are still lower than the required operation temperature of the stack and the water pump of coolant does not move, as shown in Figure 6b.
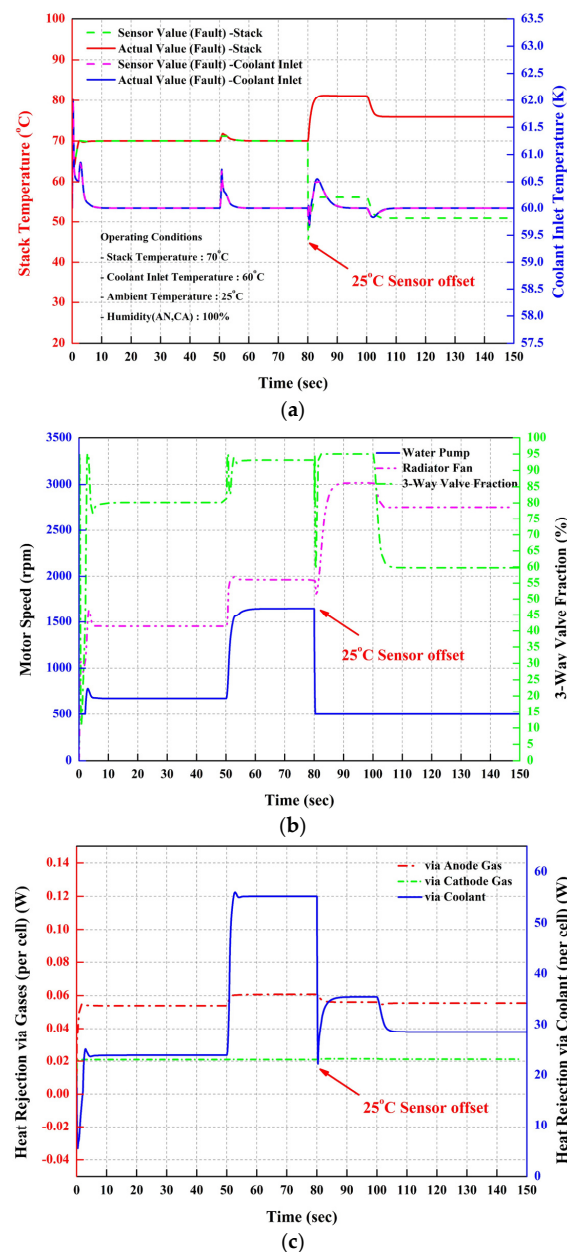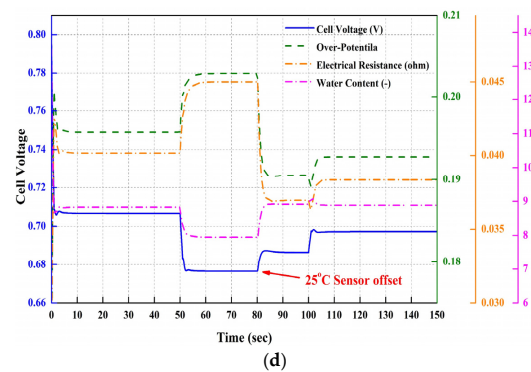

Figure 6. *Cont.*

Figure 6. Transient sensor fault behavior in PEM fuel cell under sudden stack sensor offset ((**a**) Temperature of stack and coolant inlet, (**b**) cooling components, (**c**) heat rejection in stack, (**d**) voltage responses).

When the radiator fan operates faster than in its normal state, the temperature of the coolant inlet maintains the setting value of 60 °C. As a result, the actual stack temperature is maintained, even though the stack sensor 25 °C offset fault break started at 80 s, as shown in Figure 6a. Figure 6c shows the heat transfer effect from the stack caused by anode and cathode reactants and coolant. The heat transfer by the coolant dramatically decreased because the water pump was not properly operated, which led to lower coolant flowrate due to the 25 °C offset fault of the stack temperature sensor. The heat transfer by the anode gas was also reduced for the same reason. Figure 6d shows the effects of the 25 °C offset fault on the cell voltage, over-potential, electric resistance, and water content. The value of cell voltage variation can be clearly seen; it differs according to the operation temperature of the stack, as shown in Figure 6d. The offset fault of the stack temperature sensor caused cell voltage increase due to higher operation temperature of the stack, which affects the water content, the partial pressure of reactant gases, and the electrical capacitance. As a result, the thermal management of the fuel cell system should be adequately completed.

4.6. Coolant Inlet Sensor Stuck

The dynamic effect of the fuel cell system under stuck fault in the coolant temperature sensor was examined, as shown in Figure 7, with the actual stack and coolant inlet temperature outputs, sensor outputs of the stack, and coolant inlet temperature values that were obtained. The coolant temperature sensor stuck fault (25 °C) started at time 80 s. First, the actual stack temperature and actual coolant inlet temperature are indicated; it can be observed in Figure 7a that the actual stack temperature value increased to more than 102.2 °C, and the actual coolant inlet temperature value also rose to 100 °C because of the continuous maximum operation of the water pump, as shown in Figure 7b. When the stuck fault occurs in the coolant inlet sensor, the radiator fan pump does not operate anymore because the sensor output of the coolant inlet is lower than the desired control temperature (60 °C), as shown in Figure 7b. Since the coolant inlet temperature sensor suffers a stuck fault, the actual coolant inlet temperature increased dramatically over the desired control target value (60 °C). As a result, the stack operation temperature was not controlled, even though the water pump was operating, because the radiator fan had stopped. Figure 7b shows the effect of the coolant temperature sensor stuck fault on the water pump, radiator fan, and three-way valve operation. Since the coolant temperature is lower, the radiator fan stopped and the three-way valve closed; however, the water pump runs faster, trying to lower the stack temperature by increasing the coolant flow rate. Figure 7c shows the dynamic responses of the heat rejection via gases and water coolant. Because of the decreased flow rate of the coolant and higher temperature of the actual coolant inlet temperature, the heat rejection by the coolant decreases. Figure 7d shows the responses of the cell voltage, over-potential, electric resistance, and water content corresponding to stuck fault condition in the coolant inlet temperature sensor. It is clear that the output voltage changes after each load change. The electric resistance and over-potential decrease and the increase in water content is relatively greater than the increase in cell voltage caused by increasing

stack operation temperature. Then, when the stuck fault occurs in the coolant sensor, the cell voltage increases more than in the stack sensor stuck case, which could result from the dependent effects of the higher stack temperature and the greater water content. This is because the cell voltage is affected by the stack temperature, which could induce high voltage at high stack temperature.
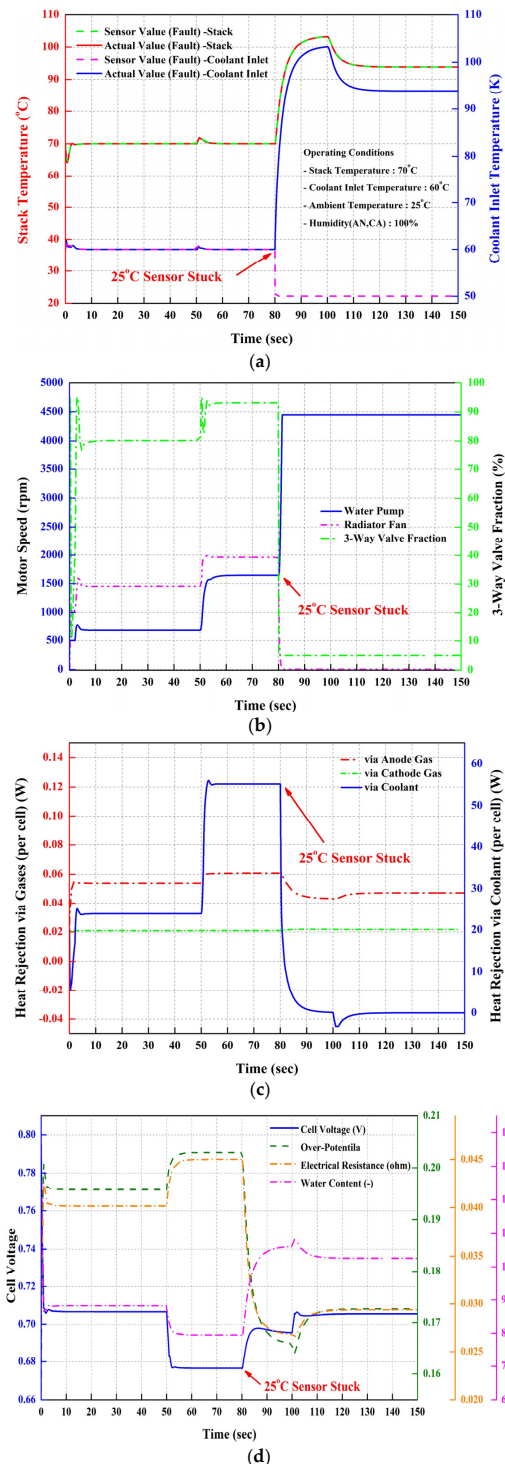

Figure 7. Transient sensor fault behavior in PEM fuel cell under sudden coolant inlet sensor stuck ((**a**) Temperature of stack and coolant inlet, (**b**) cooling components, (**c**) heat rejection in stack, (**d**) voltage responses).

4.7. Coolant Inlet Sensor Scaling

The dynamic results of the fuel cell system with scaling fault on the coolant inlet temperature sensor were studied, with results shown in Figure 8; the actual output values of the stack temperature and coolant inlet temperature, the inlet temperature value of the coolant sensor, and the sensor output of the stack coolant were obtained. The 50% scaling fault of the coolant inlet temperature sensor was applied at a time of 80 s. The actual coolant inlet temperature increased until 103.4 °C, while the actual temperature of the stack also increased to 103.4 °C, as shown in Figure 8a, since the radiator fan was operated continuously, as shown in Figure 8b. When the 50% scaling fault of the coolant sensor occurs, the temperature value from the coolant inlet temperature sensor is still below 60 °C, which is the desired temperature of the coolant inlet. As a result, the radiator fan keeps operating to reduce the coolant temperature, but the water pump does not operate to lower the stack operation temperature, as shown in Figure 8b.
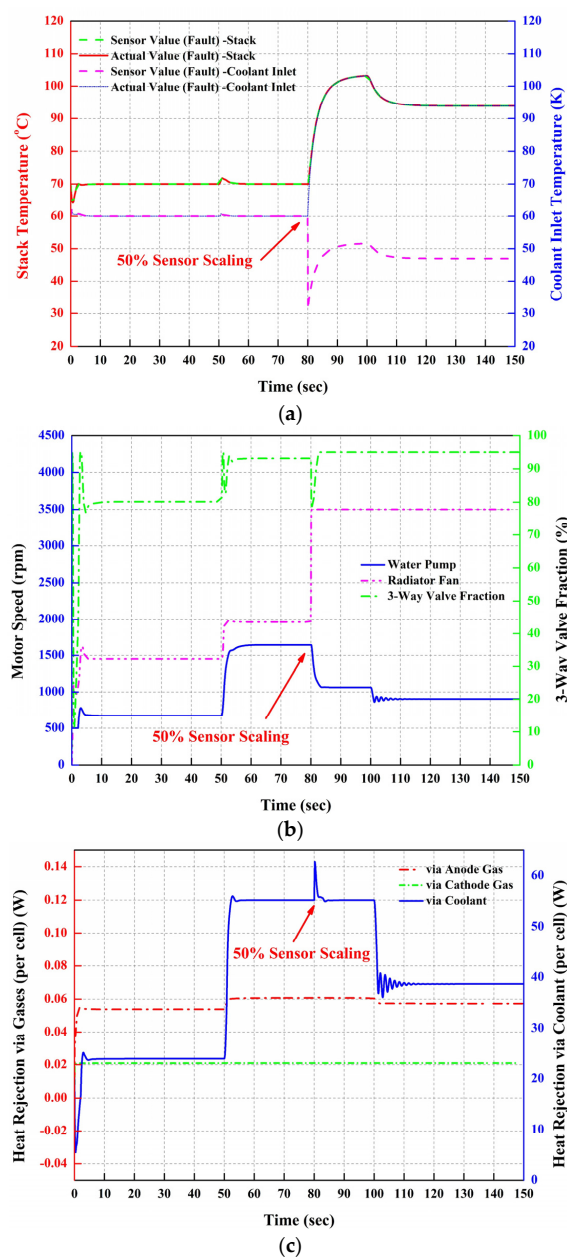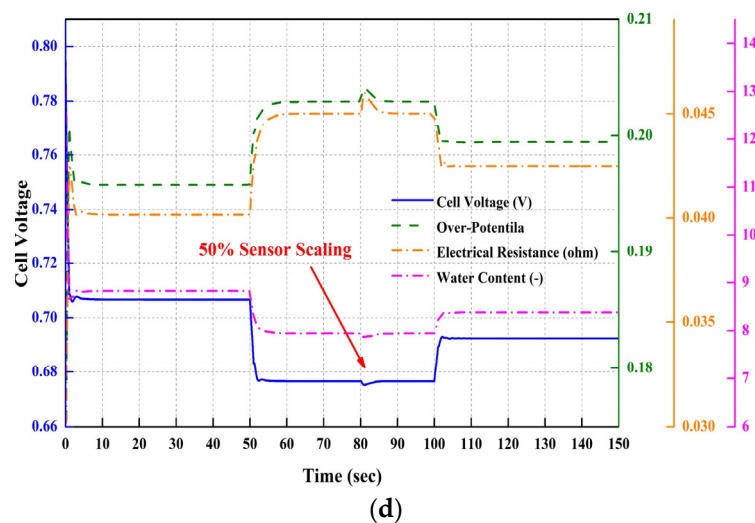

Figure 8. *Cont.*

(d)

Figure 8. Transient sensor fault behavior in PEM fuel cell under sudden coolant inlet sensor scaling ((**a**) Temperature of stack and coolant inlet, (**b**) cooling components, (**c**) heat rejection in stack, (**d**) voltage responses).

Figure 8c shows the heat rejection from the stack by anode and cathode gases and coolant. The heat rejection by anode gas decreased because the coolant temperature sensor was at 50% scaling fault. As the water pump and radiator fan operate continuously due to the higher stack temperature and coolant temperature, heat rejection by coolant was maintained first and then lowered to maintain the temperatures, which are not actually the desired operation temperatures of the stack and coolant. Figure 8d shows the responses of the cell voltage, over-potential, electric resistance, and water content corresponding to the 50% scaling fault of the coolant inlet temperature sensor. The cell voltage change is clearly seen and is affected by the stack operation temperature, as shown in Figure 8d. The 50% scaling fault of the coolant inlet temperature sensor caused cell voltage rise under higher operation temperature of the stack, which influences the water content, partial pressure of reactant gases, and electrical capacitance. This is because the cell voltage is affected by the stack temperature, which can have a high value at high stack temperature. However, in this case, when the stack temperature is raised above a certain value, the cell voltage decreases due to the electrical resistance and over-potential. As the operation temperature of the stack is increased, electrical resistance decreases. On the other hand, when the operation temperature of the stack decreases, electrical resistance increases. In conclusion, if the stack temperature exceeds the critical temperature value, cell voltage decreases due to high electrical resistance.

4.8. Coolant Inlet Sensor Offset

Figure 9 shows various values affected by the fault of the coolant temperature sensor due to a problem in which values of the sensor are measured and found to be 25 °C lower than the actual coolant inlet temperature. Comparisons between the actual results of the stack and coolant temperatures and sensor results of the stack and coolant temperatures are shown in Figure 9a. The 25 °C offset fault of the coolant temperature sensor starts at 80 s. Since the sensor has an error, the actual temperature of the coolant inlet increased to 81.2 °C and the stack operation temperature also rose to 85 °C. Then stack operation temperature and coolant inlet temperature were maintained at higher than desired temperatures. Because of the higher stack temperature, the water pump operates faster than in a normal operation to cool the stack, as shown in Figure 9b. Since the coolant sensor gives a 25 °C lower value than the actual coolant temperature, the radiator fan does not operate properly and the coolant temperature cannot be maintained at the desired value. Figure 9c shows the effects of heat transfer from the stack caused by anode and cathode reactants and coolant. The heat transfer by the coolant dramatically decreased because the radiator fan was not properly operated, which led to higher

coolant inlet temperature due to the 25 °C offset fault of the coolant inlet temperature sensor. The heat transfer by the anode gas also decreased for the same reason. Figure 9d shows the effect of the 25 °C offset fault on the cell voltage, over-potential, electric resistance, and water content. The value of cell voltage variation can be clearly seen to differ with the operation temperature of the stack, as shown in Figure 9d. The 25 °C offset fault of the coolant inlet temperature sensor caused cell voltage increase by higher operation temperature of the stack, which affects the water content, partial pressure of reactant gases, and electrical capacitance. Increased operation temperature of the stack caused the lower over-potential and electrical resistance and higher water content. As a result, the thermal management of the fuel cell system should be adequately completed.
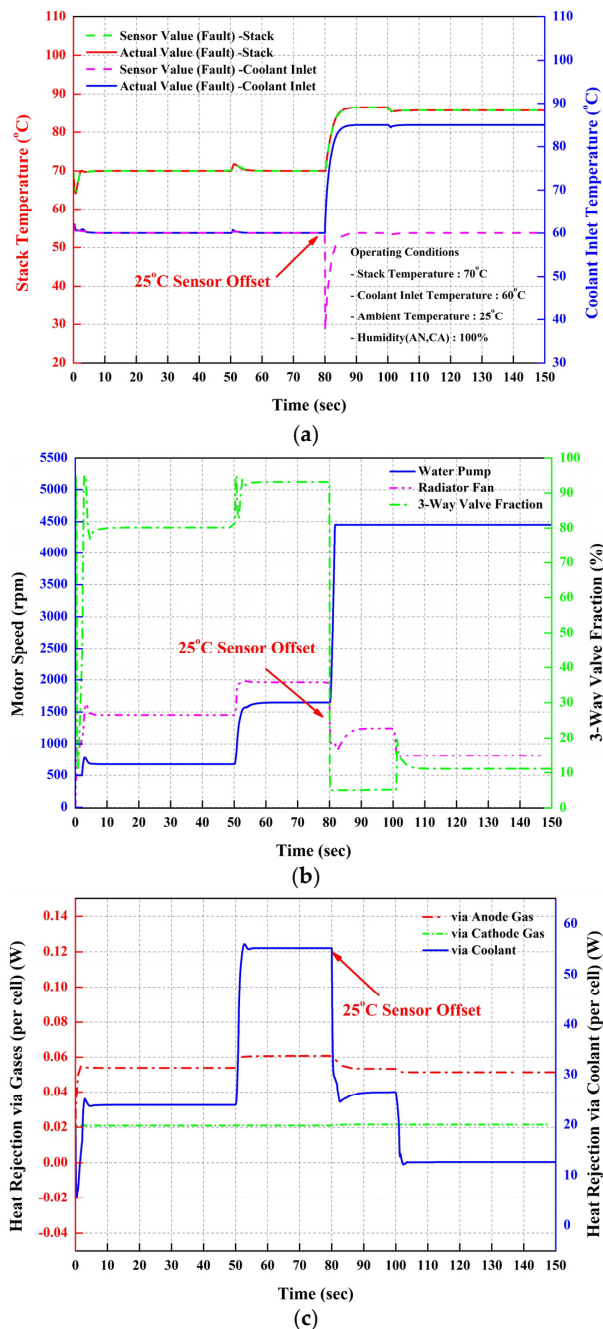

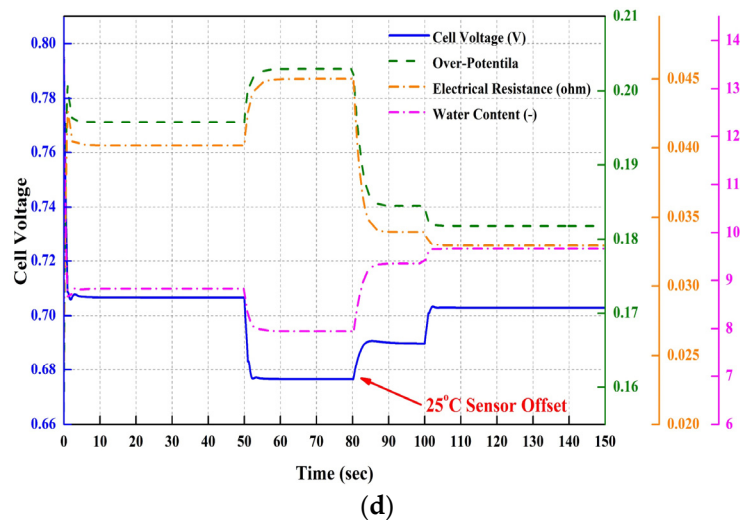(a)

(b)

(c)

Figure 9. *Cont.*

(**d**)

Figure 9. Transient sensor fault behavior in PEM fuel cell under sudden coolant inlet sensor offset ((**a**) Temperature of stack and coolant inlet, (**b**) cooling components, (**c**) heat rejection in stack, (**d**) voltage responses).

4.9. Discussions

Thus far, the results show information about the transient behaviors of the thermal management system when a sensor fault occurs due to sensor failure. To quantitatively compare the failure free and failure states, the net power of the fuel cell system is compared in this section. The gross power of the fuel cell system, and the parasitic power such as blower loss, fan loss, and water pump loss, can be obtained as

$$P_{gross} = n_{cell}E_{cell}I \tag{28}$$

$$P_{blo} = \frac{\dot{m}_{air}c_{p,air}T_{amb}\left(\left(p_{blo,o}/p_{amb}\right)^{(\gamma-1)/\gamma} - 1\right)}{\eta_{blo}} \tag{29}$$

$$P_{fan} = \frac{\dot{m}_{air}c_{p,air}T_{amb}\left(\left(p_{fan,o}/p_{amb}\right)^{(\gamma-1)/\gamma} - 1\right)}{\eta_{fan}} \tag{30}$$

$$P_{pump} = \frac{\dot{m}_{cool}\Delta p_{cool}}{\eta_{pump}\rho_{cool}} \tag{31}$$

The net power of the fuel cell system is given by

$$p_{net} = p_{gross} - p_{blo} - p_{pump} - p_{fan} \tag{32}$$

As shown in Figure 10, the net power of the fault scenario is lower than the net power of the fault-free case. Thus, when the current load changes, the fault-free case is shown to maintain the maximum net power at a level higher than that in the fault scenario. Especially, the net power of faulty system is 45.9 kW. On the other hand, the net power of fault free system is 46.1 kW. Therefore, the calculation shows that the net power of the fault-free case is about 0.2 kW higher than the fault system. Therefore, sensor failure of the fuel cell system reduces the net power of the fuel cell system, and as a result, the fault tolerance control needed to save more energy. In future studies, we plan to study fault detection, isolation, diagnosis, and tolerance control.
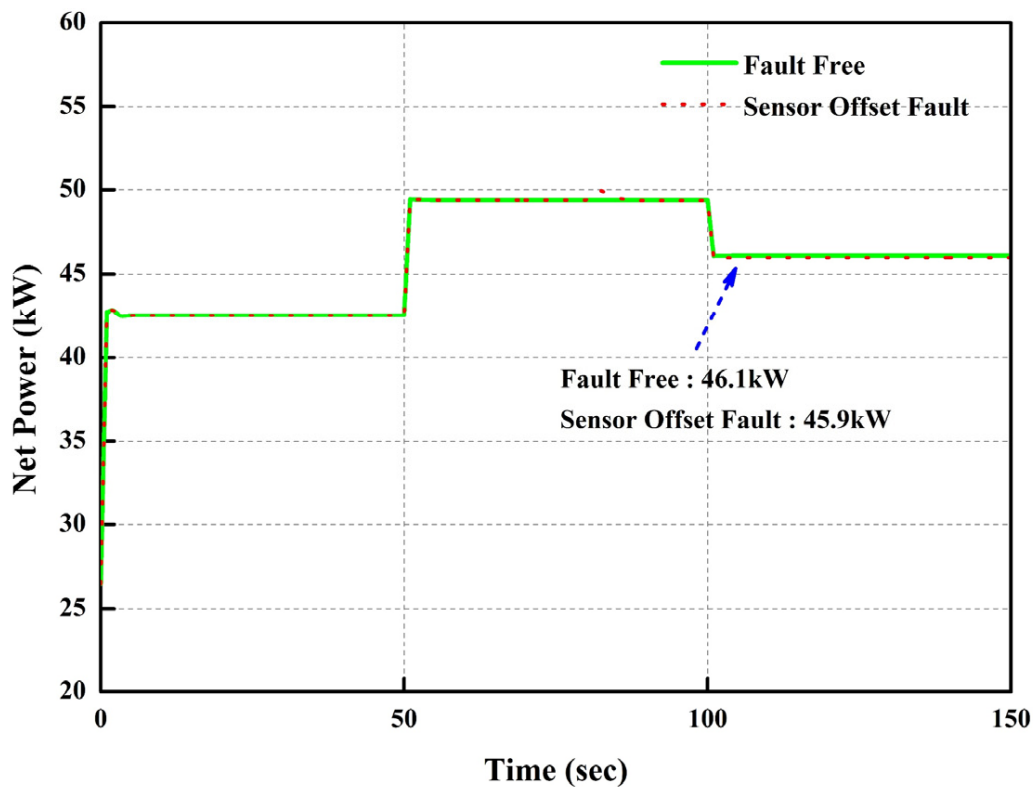
Figure 10. Comparison of net power: Fault-Free Case vs. Sensor Offset Fault.

5. Conclusions

In this study, dynamic system modeling was developed to better understand the transient behavior of a fuel cell system when sensor failure occurs. The whole fuel cell system is divided into five control volumes, i.e., anode control volume, cathode control volume, fuel cell stack, thermal management control volume, and fault signal. The governing equations of energy and continuity are used to understand the transient responses between the five volumes, including during basic fault sensor scenarios. The developed modes were simulated to investigate the transient responses when different fault scenarios are induced in the temperature sensor.

Based on the above investigation, a simple but useful fault avoidance control strategy can be designed in which a temperature sensor fault affects the whole fuel cell system. By investigating the transient responses in the system for irregular fault signals, it was found that a fault tolerant controller can be designed with fast recovery speed. Compared to the net power between the fault-free system and the faulty system, the system net power with fault signal is about 0.2kW lower than that in the fault-free system.

Nomenclature

A	**Area (*m²*)**
C	Concentration (*mol/m³*)
c_p	Specific heat (*J/kg·K*)
D	Hydraulic diameter (*m*)
E	Electric potential (*V*)
F	Faraday constant (*coulombs/electron-mol*)
f	Friction loss (-)
H	Enthalpy (*J/mol*)
h	Heat transfer coefficient (*W/m²·k*)
I	Current (*A*)
j	Current density (*A/cm²*)
k	Heat conductivity (*W/mK*)
M	Molecular weight of gas (*g/mol*)
m	Mass flow rate (*kg/s*)
N	Motor rpm (*rpm*)
Nu	Nusselt number (-)
n	Number of cells (-)
P	Power (*kW*)
p	Pressure (*Pa*)
Pr	Prandtl number (-)
Q	Heat transfer rate (*J/s*)
R	Resistance (*Ω·cm²*)
Re	Reynolds number (-)
s	Stoichiometric (-)
T	Temperature (K)
V	Volume (*m³*)
z	Thickness (*m*)

Subscripts and Superscripts

act	**Activation Loss**
air	Air
an	Anode
amb	Ambient
bip	Bipolar
blo	Blower
ca	Cathode
cell	Cell
ch	Channel
con	Concentration loss
cool	Coolant
ele	Electricity
fan	Radiator fan
gen	Generation
gas	Gas
gross	Gross power
grp	Graphite
H_2	Hydrogen
H_2O	Water
in	Inlet
L	Limit
l	Liquid
mem	Membrane
Nern	Nernst equation
N_2	Nitrogen
ohm	Ohmic loss
out	Outlet
O_2	Oxygen
pump	Water pump
react	Reaction
rev	Reservoir
st	Storage
sto	Stoichiometric
sur	Surrounding
v	Vapor

Greek

γ	**Ratio of Specific Heat**
η	Efficiency
λ	Water content
ρ	Density
σ	Bulk electronic conductivity
φ	Tuning factor

References

1. Wang, T.; Chen, K.S.; Mishler, J.; Cho, S.C.; Adroher, X.C. A review of polymer electrolyte membrane fuel cells: Technology, Application, and needs on fundamental research. *Appl. Energy* **2011**, *88*, 981–1007. [CrossRef]
2. Song, G.H.; Meng, H. Numerical modeling and simulation of PEM fuel cells: Progress and perspective. *Acta Mech. Sin.* **2013**, *29*, 318–334. [CrossRef]
3. Wu, H.W. A review of recent development: Transport and performance modeling of PEM fuel cells. *Appl. Energy* **2016**, *165*, 81–106. [CrossRef]
4. Kim, Y.B.; Kang, S.J. Time delay control for fuel cells with bidirectional DC/DC converter and battery. *Int. J. Hydrog. Energy* **2010**, *35*, 8792–8803. [CrossRef]
5. Xu, L.; Hong, P.; Fang, C.; Li, J.; Ouyang, M.; Lehnert, W. Interactions between a polymer electrolyte membrane fuel cell and boost converter utilizing a multiscale model. *J. Power Sources* **2018**, *395*, 237–250. [CrossRef]
6. Amiri, A.; Tang, S.; Steinberger-Wilckens, R.; Tadé, M.O. Evaluation of fuel diversity in solid oxide fuel cell system. *Int. J. Hydrog. Energy* **2018**, *43*, 23475–23487. [CrossRef]
7. Ma, T.; Yang, Y.; Lin, W.; Yang, Y.; Jia, W.; Zhang, J. Design of a novel high-efficiency water separator for proton exchange membrane fuel cell system. *Int. J. Hydrog. Energy* **2019**, *44*, 5462–5469. [CrossRef]
8. Zhang, B.; Lin, F.; Zhang, C.; Liao, R.; Wang, Y.X. Design and implementation predictive control for an open cathode fuel cell thermal management system. *Renew. Energy* **2020**, *154*, 1014–1024. [CrossRef]
9. Zhou, Z.; Qiu, D.; Zhai, S.; Peng, L.; Lai, X. Investigation of the assembly for high-power proton exchange membrane fuel cell stack through an efficient equivalent model. *Appl. Energy* **2020**, *277*, 115532. [CrossRef]
10. Liese, E.; Albright, J.; Zitney, S.A. Startup, shutdown, and load-following simulations of a 10 MWe supercritical CO_2 recompression closed Brayton cycle. *Appl. Energy* **2020**, *227*, 115628. [CrossRef]
11. Gallo, M.; Costabile, C.; Sorrentino, M.; Polverino, P.; Pianese, C. Development and application of a comprehensive model-based methodology for fault mitigation of fuel cell powerd systems. *Appl. Energy* **2020**, *279*, 115698. [CrossRef]
12. Batet, D.; Zohra, F.T.; Kristensen, S.B.; Andreasen, S.J. Continuous durability study of a high temperature polymer electrolyte membrane fuel cell stack. *Appl. Energy* **2020**, *277*, 115588. [CrossRef]
13. Shahgaldi, S.; Alaefour, I.; Li, X. The impact of short side chain ionomer on polymer electrolyte membrane fuel cell performance and durability. *Appl. Energy* **2018**, *217*, 295–302. [CrossRef]
14. Lan, T.; Strunz, K. Modeling of multi-physics transients in PEM fuel cells using equivalent circuits for consistent representation of electric, pneumatic, and thermal quantities. *Electr. Power Energy Syst.* **2020**, *119*, 105803. [CrossRef]
15. He, P.; Mu, Y.U.; Park, J.W.; Tao, W.Q. Modeling of the effects of cathode catalyst layer design parameters on performance of polymer electrolyte membrane. *Appl. Energy* **2020**, *277*, 115555. [CrossRef]
16. Liu, B.; Chen, H.; Zhang, T.; Pei, P. A vehicular proton exchange membrane fuel cell system co-simulation modeling method based on the stack internal distribution parameters monitoring. *Energy Convers. Manag.* **2019**, *197*, 111898. [CrossRef]
17. Messing, M.; Kjeang, E. Empirical modeling of cathode electrode durability in polymer electrolyte fuel cells. *J. Power Sources* **2020**, *451*, 227750. [CrossRef]
18. Pan, M.; Li, C.; Liao, J.; Lei, H.; Pan, C.; Meng, X.; Huang, H. Design and modeling of PEM fuel cell based on different flow fields. *Energy* **2020**, *207*, 118331. [CrossRef]
19. Gwak, G.; Ju, H. A rapid start-up strategy for polymer electrolyte fuel cells at subzero temperature based on control of the operating current density. *Int. J. Hydrog. Energy* **2015**, *40*, 11989–11997. [CrossRef]

20. Murugesan, K.; Senniappan, V. Investigation of water management dynamics on the performance of a Ballard-Mark-V proton exchange membrane fuel cell stack system. *Int. J. Electrochem. Sci.* **2013**, *8*, 7885–7904.
21. Lee, C.H.; Yang, J.T. Modeling of the Ballard-Mark-V proton exchange membrane fuel cell with power converters for applications in autonomous underwater vehicles. *J. Power Sources* **2011**, *196*, 3810–3823. [CrossRef]
22. Kim, M.S.; Kim, D.K. Parametric study on dynamic heat and mass transfer response in polymer electrolyte membrane fuel cell for automotive applications. *Appl. Therm. Eng.* **2020**, *167*, 114729. [CrossRef]
23. Kim, Y.S.; Kim, D.K. Operating strategy for successful start-up in self-humidified polymer electrolyte membrane fuel-cell system. *Appl. Therm. Eng.* **2019**, *152*, 370–376. [CrossRef]
24. Pan, T.; Shen, J.; Sun, L.; Lee, K.Y. Thermodynamic modelling and intelligent control of fuel cell anode purge. *Appl. Therm. Eng.* **2019**, *154*, 196–207. [CrossRef]
25. Chen, B.; Tu, Z.; Chan, S.H. Performance degradation and recovery characteristics during gas purging in a proton exchange membrane fuel cell with a dead-ended anode. *Appl. Therm. Eng.* **2018**, *129*, 968–978. [CrossRef]
26. Mao, L.; Jackson, L.; Davies, B. Investigation of PEMFC fault diagnosis with consideration of sensor reliability. *Int. J. Hydrog. Energy* **2018**, *43*, 16941–16948. [CrossRef]
27. Steiner, N.Y.; Hissel, D.; Mocoteguy, P.; Candusso, D. Diagnosis of polymer electrolyte fuel cells failure modes (flooding & drying out) by neural network modeling. *Int. J. Hydrog. Energy* **2011**, *36*, 3067–3075.
28. Bougatef, Z.; Abdelkrim, N.; Aitouche, A.; Abdelkrim, M.N. Fault detection of a PEMFC system based on delayed LPV observer. *Int. J. Hydrog. Energy* **2020**, *45*, 11233–11241. [CrossRef]
29. Han, J.Y.; Yu, S.S. Ram air compensation analysis of fuel cell vehicle cooling system under driving modes. *Appl. Therm. Eng.* **2018**, *142*, 530–542. [CrossRef]
30. Han, J.Y.; Yu, S.S.; Yi, S. Advanced thermal management of automotive fuel cells using a model reference adaptive control algorithm. *Int. J. Hydrog. Energy* **2017**, *42*, 4328–4341. [CrossRef]